

Accessing the anisotropic non-thermal phonon populations in black phosphorus

Hélène Seiler,^{*,†} Daniela Zahn,[†] Marios Zacharias,^{†,‡} Patrick Hildebrandt,[†]
 Thomas Vasileiadis,[†] Yoav William Windsor,[†] Yingpeng Qi,[†] Christian
 Carbogno,[†] Claudia Draxl,[¶] Ralph Ernstorfer,[†] and Fabio Caruso^{*,§}

[†]*Fritz Haber Institute of the Max Planck Society, 14195 Berlin, Germany*

[‡]*Department of Mechanical and Materials Science Engineering, Cyprus University of
 Technology, P.O. Box 50329, 3603 Limassol, Cyprus*

[¶]*Institut für Physik and IRIS Adlershof, Humboldt-Universität zu Berlin, Berlin, Germany*

[§]*Institut für Theoretische Physik und Astrophysik, Christian-Albrechts-Universität zu Kiel,
 D-24098 Kiel, Germany*

E-mail: seiler@fhi-berlin.mpg.de; caruso@physik.uni-kiel.de

Abstract

We combine femtosecond electron diffuse scattering experiments and first-principles calculations of the coupled electron-phonon dynamics to provide a detailed momentum-resolved picture of the ultrafast lattice thermalization in a thin film of black phosphorus. The measurements reveal the emergence of highly anisotropic non-thermal phonon populations which persist for several picoseconds following excitation of the electrons with a light pulse. Combining ultrafast dynamics simulations based on the time-dependent Boltzmann formalism and calculations of the structure factor, we reproduce the experimental data and identify the vibrational modes primarily responsible for the carrier relaxation via electron-phonon coupling and the subsequent lattice thermalization via

phonon-phonon scattering. In particular, we attribute the non-equilibrium lattice dynamics of black phosphorus to highly-anisotropic phonon-assisted scattering processes, which are primarily mediated by high-energy optical phonons. Our approach paves the way towards unravelling and controlling microscopic energy-flow pathways in two-dimensional materials and van der Waals heterostructures, and may also be extended to other non-equilibrium phenomena involving coupled electron-phonon dynamics such as superconductivity, phase transitions or polaron physics.

Black phosphorus (BP) exhibits a tunable band gap in the mid-IR,¹⁻³ high carrier mobilities,⁴⁻⁶ and a layered crystal structure. These features make it a versatile platform to explore novel device concepts, such as field-effect transistors, saturable absorbers, and polarization-sensitive photodetectors.^{2,4,5,7-9} The pronounced crystal structure anisotropy of BP further underpins the emergence of strikingly anisotropic macroscopic properties, as exemplified by its thermal¹⁰⁻¹² and electrical conductivities,^{1,5,13,14} as well as its optical response.^{5,15-17}

Since practical applications based on these properties invariably exploit non-equilibrium states of either the lattice or hot carriers, it is desirable to attain a detailed understanding of the ultrafast dynamics of electronic and vibrational degrees of freedom in BP. Following photo-excitation, hot carriers relax to the band edges by transferring their excess energy to the lattice via the emission of phonons, which triggers coupled carrier-lattice non-equilibrium dynamics. Optical and photoemission spectroscopies have been employed extensively to investigate carrier-phonon scattering channels and their influence on the carrier dynamics in BP.^{14,18-25} While these techniques provide direct information on the electrons, the non-equilibrium dynamics of the lattice can only be inferred indirectly through its effects on the electronic structure. Femtosecond electron diffuse scattering (FEDS), conversely, is an ideal technique to circumvent these limitations and complement optical and photoemission spectroscopies. FEDS provides direct access to lattice dynamics and electron-phonon scattering processes with time and momentum resolution.²⁶⁻²⁸ Owing to its sensitivity to both electron-phonon and phonon-phonon scattering processes in reciprocal space, FEDS is thus

well-suited to establish a microscopic picture of the energy flow between hot electrons and the BP lattice.

Here, we combine FEDS experiments with ab-initio calculations to investigate the coupled electron-phonon dynamics in BP following photo-excitation. Our study reveals that strongly anisotropic non-thermal phonon populations are established throughout the first picoseconds of the dynamics. A regime of thermal equilibrium is only re-established by the ensuing anharmonic decay pathways (phonon-phonon coupling) on timescales of the order of 50-100 ps. To unravel the origin of the non-equilibrium lattice dynamics and its signatures in FEDS experiments, we conduct first-principles calculations of the coupled electron-phonon dynamics based on the time-dependent Boltzmann formalism, whereby electron-phonon and phonon-phonon scattering processes are explicitly accounted for. Calculations of the structure factor further enable a direct comparison with the experimental data. We show that the relaxation of excited electrons and holes is governed by the emission of high-energy optical phonons within a restricted region of the Brillouin zone, and it is responsible for the anisotropic non-thermal phonon populations revealed by FEDS.

Results and discussion

The layered orthorhombic crystal structure of BP is illustrated in Figure 1(a) and (b) from a top and side view, respectively, whereas its Brillouin zone (BZ) and main high-symmetry points (labelled according to the convention of Ref. 30) are reported in Figure 1(e). The equilibrium electron diffraction pattern of Figure 1(c) provides a direct view of the reciprocal lattice for momenta within the X- Γ -A plane in the BZ [shaded blue plane in Figure 1(e)]. Bright high-intensity features arise for transferred momenta matching the reciprocal lattice vectors \mathbf{G} , according to Bragg's law for the interference condition. These measurements are in good agreement with previous TEM experiments.³¹ Besides the pronounced anisotropy of the BP crystal lattice, marked by different structural motifs along the *armchair* and *zigzag*

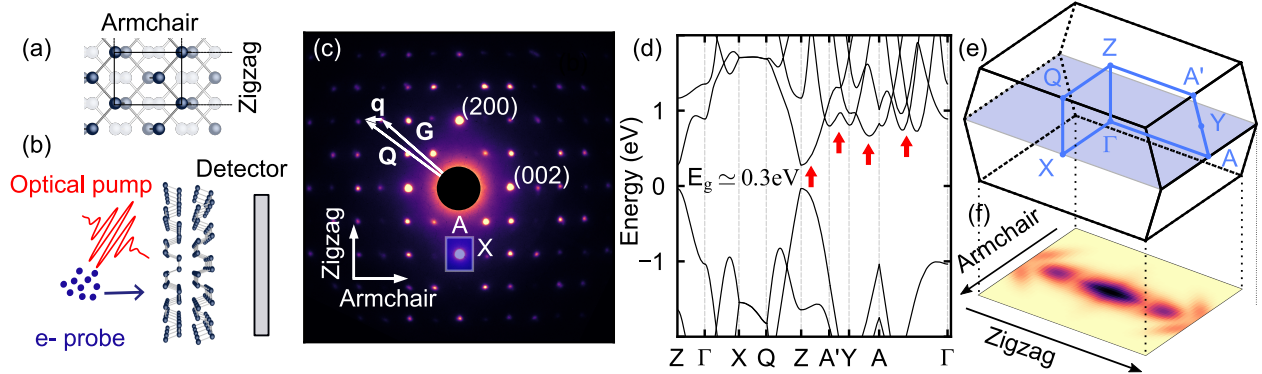


Figure 1: (a) Top view of the BP crystal lattice. (b) Schematic illustration of femtosecond electron diffuse scattering, with side view of the BP crystal lattice. (c) Representative transmission diffraction pattern of BP. The Brillouin zone can be drawn around each Bragg peak, as illustrated by the rectangle over the $(\bar{2}00)$ reflection. An arbitrary position in reciprocal space, \mathbf{Q} , can always be expressed as $\mathbf{G} + \mathbf{q}$, where \mathbf{G} is a reciprocal lattice vector and \mathbf{q} the phonon wavevector. (d) Electronic band structure as obtained from density-functional theory. A scissor shift of 0.2 eV has been applied to the conduction manifold to match the experimental band gap $E_g \simeq 0.3$ eV.²⁹ (e) Brillouin zone and high-symmetry points of BP. The blue shading marks the region of reciprocal space probed by our FEDS measurements. (f) Momentum distribution of photo-excited carriers approximated by a Fermi-Dirac function $f_{n\mathbf{k}}$ is shown (dark regions indicate more excited carriers). The colored rectangles indicate phonons groups, see text.

directions (Figure 1(a)), striking signatures of anisotropy also manifest themselves in the electronic properties.

The electronic band structure, obtained from density-functional theory and illustrated in Figure 1(d), exhibits a direct gap at the Z point and a conduction band characterized by several local minima in the vicinity of the Y, A, and A' high-symmetry points. The local minima in the conduction band thus involve crystal momenta with an in-plane component directed primarily along the zigzag direction. Conversely, no local minima arise in the conduction band along Γ -X and Z-Q (armchair direction). The anisotropic character of the band structure is shown below to influence profoundly the non-equilibrium dynamics of electrons and phonons in BP, leading to the emergence of a striking anisotropy in the phonon population following the interaction with light pulses.

Femtosecond electron diffuse scattering measurements

To investigate the non-equilibrium lattice dynamics of BP with momentum and time resolutions, we perform FEDS measurements on a free-standing thin film of BP. The sample has an estimated thickness of 39 ± 5 nm and it has been obtained by mechanical exfoliation of a bulk crystal. In FEDS, a laser pulse is employed to drive the system into an excited electronic state. After a controllable time delay t , the sample is probed by an electron pulse which diffracts off the lattice. The distribution of the diffracted electrons generated by this procedure provides a direct probe of the non-equilibrium dynamics of the lattice in reciprocal space.³² A schematic illustration of the experiment is reported in Figure 1(b). Here, the BP flake is photo-excited with a light pulse with energy $h\nu = 1.61$ eV and polarization aligned along the armchair direction. Additional measurements using a pump energy $h\nu = 0.59$ eV are reported in the Supporting Information. All measurements are performed at 100 K. The initial density of photo-excited electrons and holes induced by the pump pulse is estimated to $n_e = 7.3 \cdot 10^{13}$ cm⁻² (see Supporting Information).

Figure 2(a) illustrates the relative intensity changes of the (400) and (004) Bragg peaks – located along the zigzag (squares) and armchair (triangles) directions, respectively – throughout the non-equilibrium dynamics of the lattice. A clear fingerprint of anisotropic lattice dynamics is revealed by the different time dependence of these elastic scattering signals. The dynamics of both armchair and zigzag reflections are well-captured by bi-exponential decays, with a fast time constant of 500 fs and a slower time constant of 20 ps. This behaviour was described in detail in Ref.,³³ where some of us investigated the dynamics of the Bragg reflections in BP, revealing non-thermal phonon distributions persisting for tens of picoseconds.

To obtain a momentum-resolved picture of the non-equilibrium lattice dynamics of BP, we go beyond the analysis of the elastic scattering signals and we inspect the transient signatures of inelastic scattering processes as revealed by FEDS. The contribution of the different high-symmetry points to the FEDS intensity can be singled out by dividing the

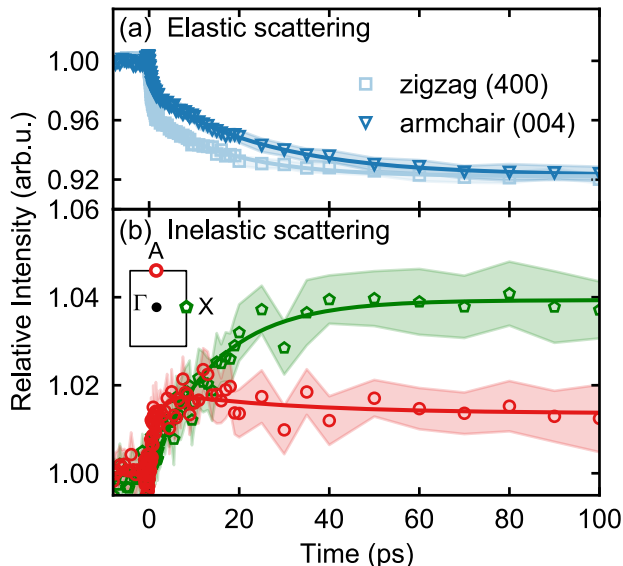


Figure 2: (a) Exemplary anisotropic elastic scattering signals for *zigzag* (squares) and *armchair* reflections (triangles). (b) diffuse scattering signal at A (circles) and X (pentagons) around the (400) reflection. The data in both panels is the average over the Friedel pair (e.g. (400) and $\bar{4}00$). The error estimates represent the standard error of the mean signal over multiple delay scans.

diffraction pattern into BZs around each Bragg reflection peak, as illustrated by the shaded rectangle in Figure 1 (c) for the $\bar{2}00$ reflection. Exemplary time-resolved FEDS signals around the (400) Bragg peak are shown in Figure 2 (b) for the A (circles) and X (pentagons) points in the BZ. As diffuse scattering occurs primarily through phonon-induced scattering processes, the signal measured at a given point \mathbf{q} in the BZ reflects the phonon population with the same momentum.^{26–28,34–36} The red curve in Figure 2 (b) indicates the relative intensity of the FEDS signal as a function of time at the A point. Similar dynamics are observed at all the investigated A points. A bi-exponential fit to the data yields a rising time constant of 1.7 ± 0.1 ps, followed by a slower relaxation of 30 ± 2 ps. We note that the 1.7 ps time constant does not appear in an elastic scattering analysis. The time evolution of the diffuse signal at X, shown in green in Figure 2 (b), reveals a drastically different phonon dynamics at the X point as compared to the A point. Fitting with an exponential function yields a time constant of 14.3 ± 0.1 ps. These measurements indicate a striking anisotropy of the transient FEDS intensity in the BZ, suggesting a highly momentum-dependent excitation

and relaxation of the lattice following photo-excitation.

A comprehensive view of transient phonon distributions in momentum space is shown in Figure 3 (a-c), at pump-probe delays of 2, 10, and 50 ps. This set of data demonstrates profound changes in the diffuse scattering signal as pump-probe delay increases, reflecting different phonon populations at different times. While the diffuse pattern at 2 ps is weak and displays faint lines in the Γ -A direction, the diffuse signal at 50 ps is more pronounced, differently shaped, and more anisotropic. A closer inspection of the changes in diffuse scattering signal around Bragg reflections, shown as insets in Figure 3 (c), reveals high anisotropy between the intensities along the two main crystal axes at 50 ps. These highly anisotropic dynamics within a given BZ, and between BZs, highlight the value of time-resolved diffuse scattering as direct probes of transient non-thermal phonon distributions in momentum space [Figure 3 (a-c)].

Theoretical modeling of non-equilibrium lattice dynamics

To gain further insight into the non-equilibrium dynamics of the lattice, we perform first-principles calculations of the coupled electron-phonon dynamics of BP based on the time-dependent Boltzmann equations:³⁷

$$\partial_t f_{n\mathbf{k}}(t) = \Gamma_{n\mathbf{k}}^{\text{ep}}[f_{n\mathbf{k}}(t), n_{\mathbf{q}\nu}(t)] \quad (1)$$

$$\partial_t n_{\mathbf{q}\nu}(t) = \Gamma_{\mathbf{q}\nu}^{\text{pe}}[f_{n\mathbf{k}}(t), n_{\mathbf{q}\nu}(t)] + \Gamma_{\mathbf{q}\nu}^{\text{pp}}[n_{\mathbf{q}\nu}(t)] \quad (2)$$

Here, $\partial_t = \partial/\partial t$, $f_{n\mathbf{k}}$ denotes the electron distribution function for electron band index n and electron momentum \mathbf{k} , and $n_{\mathbf{q}\nu}$ the phonon distribution function for wavevector \mathbf{q} and branch index ν . Equations (1) and (2) account seamlessly for the effects of electron-phonon and phonon-phonon scattering on the ultrafast dynamics of electrons and phonons with momentum resolution. The influence of the electron-phonon interaction on $f_{n\mathbf{k}}$ ($n_{\mathbf{q}\nu}$) is accounted for by the collision integral $\Gamma_{n\mathbf{k}}^{\text{ep}}$ ($\Gamma_{\mathbf{q}\nu}^{\text{pe}}$), whereas the phonon-phonon scattering

due to lattice anharmonicities is accounted for via $\Gamma_{\mathbf{q}\nu}^{\text{pp}}$. In short, Eqs. (1) and (2) have been solved for electron (phonon) momenta within the Q-Z-A' (X- Γ -A) plane in the BZ by time-stepping the time derivative with intervals of 1 fs for a total simulated time of 100 ps (10^5 time steps), with the collision integrals being recomputed at each time step. A detailed account of the numerical implementation and explicit expressions for the collision integrals have been reported elsewhere.³⁷

As initial condition for the time propagation, we consider an electronic excited state characterized by a density n of electrons and holes excited to the conduction and valence bands, respectively. This state is realized by defining electronic occupations in the conduction band according to $f_{n\mathbf{k}}^0(\mu_e, T_{\text{el}}^0) = [e^{(\varepsilon_{n\mathbf{k}} - \mu_e)/k_{\text{B}}T_{\text{el}}^0} + 1]^{-1}$. μ_e is the chemical potential of the electrons in the conduction band, which is obtained by solving the integral equation $n = \Omega_{\text{BZ}}^{-1} \sum_m^{\text{cond.}} \int d\mathbf{k} f_{m\mathbf{k}}^0(\mu_e, T_{\text{el}}^0)$, where $n = 7.3 \cdot 10^{13} \text{ cm}^{-2}$ is the density of photo-excited carriers estimated in the experiment (see Supporting Information). A similar treatment is applied to holes in the valence band. The initial electronic temperature $T_{\text{el}}^0 = 7000 \text{ K}$ is related to the excess energy of the excited electrons and holes, and it is chosen such that the final vibrational temperature of the lattice after thermalization $T_{\text{fin}}^{\text{vib}}$ matches the experimental estimate of 300 K. The lattice is initially at thermal equilibrium, with phonon occupations defined according to the Bose-Einstein statistics $n_{\mathbf{q}\nu}^{\text{BE}} = [e^{\hbar\omega_{\mathbf{q}\nu}/k_{\text{B}}T} - 1]^{-1}$, at the same temperature of experiments $T = 100 \text{ K}$.

From the phonon distribution function $n_{\mathbf{q}\nu}(t)$, we can calculate the momentum-resolved effective vibrational temperature of the lattice $\tilde{T}_{\mathbf{q}} = N_{\text{ph}}^{-1} \sum_{\nu} T_{\mathbf{q}\nu}$, where $N_{\text{ph}} = 12$ is the number of phonon branches of BP and $T_{\mathbf{q}\nu} = \hbar\omega_{\mathbf{q}\nu} \{k_{\text{B}} \ln[1 + n_{\mathbf{q}\nu}(t)]\}^{-1}$. In Figure 4(a)-(f), we report $\tilde{T}_{\mathbf{q}}$ at different time steps of the coupled electron-phonon dynamics for crystal momenta within the X- Γ -A plane of the BZ (shaded blue in Figure 1(e), corresponding to the plane probed in the FEDS experiments). Before excitation ($t < 0$), the constant temperature $\tilde{T}_{\mathbf{q}} = 100 \text{ K}$ in the BZ reflects thermal equilibrium. At $t = 0.1 \text{ ps}$, red features in Figure 4(b) indicate the enhancement in the phonon population around Γ (zone center) and along the

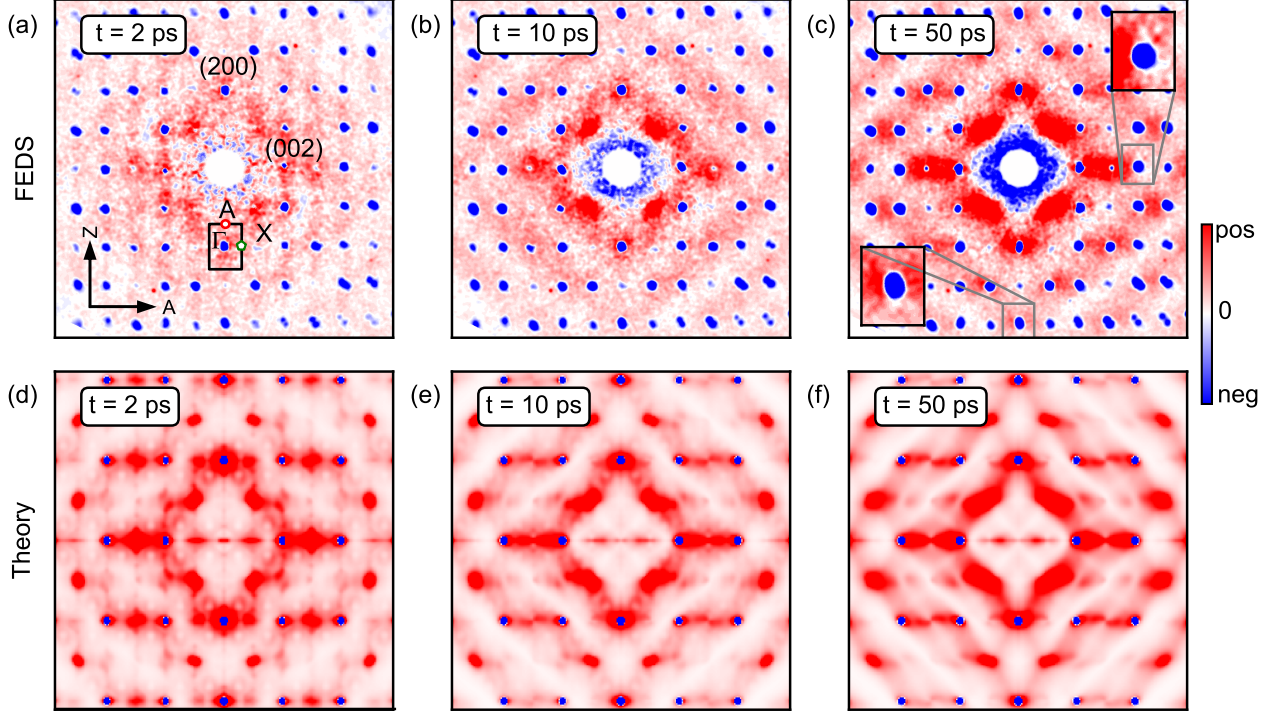


Figure 3: (a-c) Momentum-resolved electron diffraction signals, $I(\mathbf{Q}, t) - I(\mathbf{Q}, t \leq t_0)$, at pump-probe delays of 2 ps, 10 ps, and 50 ps. Two-fold symmetrized data,³⁸ raw data shown in Supporting Information. The Bragg reflections (blue dots) are negative due to the Debye-Waller effect. The diffuse background (red) qualitatively evolves as a function of pump-probe delay. Selected Brillouin zones are shown in inset for the (004) and the $(\bar{4}00)$ reflections on the 50 ps map. All data are normalized to a common number. (d-f) Simulated non-equilibrium scattering signals at pump-probe delays of 2 ps, 10 ps, and 50 ps. The phonon temperatures are based on the non-thermal model described in the text and shown in Figure 4 (a). All data are normalized to a common number.

Γ -A high-symmetry line. This anisotropy becomes more pronounced at later times, as shown in Figure 4(c) and (d) for $t = 0.5$ and 2.5 ps, respectively. As anticipated above, the origin of this behaviour is related to the anisotropy of the valence and conduction bands.

Owing to the absence of local minima in conduction band along the armchair direction (i.e., Γ -X and Z-Q), the photo-excited electrons are constrained to occupy states with crystal momenta along the zigzag direction, i.e., where the available local minima are located (arrows in Figure 1 (d)). This scenario is illustrated by highly-anisotropic electronic occupations $f_{n\mathbf{k}}^0$ in the conduction band, reported in Figure 1 (f) for the initial electronic excited state defined above, arising from the partial filling of the available low-energy states. Due to momentum

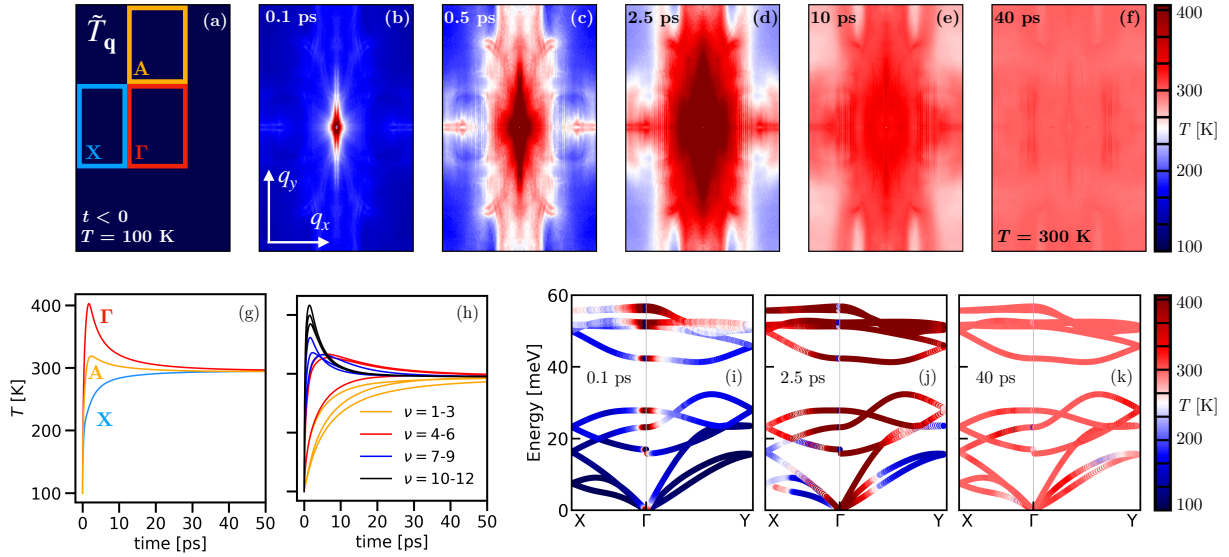


Figure 4: (a) Effective vibrational temperature $\tilde{T}_{\mathbf{q}}$ for crystal momenta in the X- Γ -A plane of the Brillouin zone before excitation ($t < 0$), and at several time delays throughout the non-equilibrium dynamics of the lattice (b-f). (g) Time-dependence of $\tilde{T}_{\mathbf{q}}$ for momenta around the high-symmetry points Γ (red), A (yellow), and X (blue). Each curve has been obtained by averaging $\tilde{T}_{\mathbf{q}}$ for momenta within the regions highlighted in (a) at each time step. (h) Time-dependence of the branch-resolved vibrational temperature T_{ν} (averaged over momentum). $\nu = 1 - 3$ denote the acoustic branches, $\nu = 10 - 12$ the highest-energy optical phonons, etc. (i-k) Branch and momentum resolved effective vibrational temperatures, superimposed to the phonon dispersion as a color coding, for $t = 0.1$ (i), 2.5 (j), and 40 ps (k).

conservation, the relaxation of carriers to the conduction band minimum (Z point) thus entails a predominant emission of phonons with momenta \mathbf{q} along the Γ -A directions. Based on this picture, the anisotropic increase of the vibrational temperature in the BZ reflects the phase-space constraints in the electron-phonon interactions, and thus in the relaxation path of photo-excited electrons and holes. For $t = 10$ ps (Figure 4 (d)), the anisotropy of the vibrational temperature in the BZ is significantly reduced. On these timescales, phonon-phonon scattering – accounted for via Γ^{pp} in Eq. (2) – counteracts the effects of the electron-phonon scattering by driving the lattice towards thermal equilibrium. For $t = 40$ ps (Figure 4 (d)), thermal equilibrium is re-established at the temperature $T_{\text{vib}}^{\text{fin}} = 300$ K.

To gain further insight into the anisotropy of the lattice dynamics, we illustrate in Figure 4(g) the time dependence of the vibrational temperature $\tilde{T}_{\mathbf{q}}$ around the X, Γ , and A

regions (obtained by averaging $\tilde{T}_{\mathbf{q}}$ over the rectangles in Figure 4(a)) throughout the first 50 ps of the dynamics. For momenta around Γ and A, the temperature reaches a maximum at 1.7 and 2.3 ps, respectively, whereas no maximum is observed around X. These timescales indicate the time required for the electrons to transfer energy to the lattice via electron-phonon scattering. The good agreement with the experimental time constant of 1.7 ps extracted from the rise of the FEDS intensity at A (Figure 2(b)), suggests that transient changes of the FEDS intensities for timescales smaller than 2 ps reflect primarily the energy transfer from the electrons to the lattice driven by the electron-phonon coupling.

In Figure 4(h), we report the average vibrational temperature for each phonon branch ($\tilde{T}_{\nu} = \Omega_{\text{BZ}}^{-1} \int d\mathbf{q} T_{\mathbf{q}\nu}$) throughout the first 50 ps, whereas the vibrational temperatures superimposed to the phonon dispersion is illustrated in Figure 4(i-k). Because the contribution of each phonon mode to the carrier relaxation is dictated by its coupling strength, modes characterized by stronger coupling provide a preferential decay channel for the excited electrons and thus exhibit a higher vibrational temperature throughout the initial stages of the dynamics. In particular, Figures 4(h)-(k) indicate that the electron relaxation is dominated by the high-energy optical phonons, whereby the out-of-phase vibration of P atoms in the lattice leads to the largest electron-phonon coupling strength.

To inspect directly the influence of the non-equilibrium lattice dynamics on the scattering intensity probed in the FEDS experiments, we conduct first-principles calculations of the structure factor by explicitly accounting for the influence of electron-phonon interactions and anisotropic population of the vibrational modes in the unit cell. Specifically, we perform computations of the *all-phonon* structure factor $I_{\text{all}}(\mathbf{Q}, T)$.^{39,40} Indeed we find that taking into account multi-phonon effects is essential for an accurate reproduction of the experimentally observed diffraction patterns of BP seen in Figures 3(a-c). The expression for $I_{\text{all}}(\mathbf{Q}, T)$ reads:

$$I_{\text{all}}(\mathbf{Q}, T) = N_p \sum_{\kappa\kappa'} f_{\kappa}(\mathbf{Q}) f_{\kappa'}^*(\mathbf{Q}) e^{-W_{\kappa\kappa'}(\mathbf{Q}, T)} \sum_p e^{i\mathbf{Q} \cdot [\mathbf{R}_p + \boldsymbol{\tau}_{\kappa} - \boldsymbol{\tau}_{\kappa'}]} e^{P_{p, \kappa\kappa'}(\mathbf{Q}, T)}. \quad (3)$$

Here N_p is the number of \mathbf{q} -points used to sample the first Brillouin Zone, $f_\kappa(\mathbf{Q})$ denotes the scattering amplitude of atom κ , $W_{\kappa\kappa'}(\mathbf{Q}, T)$ is the Debye-Waller factor, τ_κ represents the atomic positions and \mathbf{R}_p defines the position vector of unit cell p contained in a Born-von Kármán supercell. The phononic factor, $e^{P_{p,\kappa\kappa'}(\mathbf{Q}, T)}$, includes all orders of phonon processes and its exponent is given by:

$$P_{p,\kappa\kappa'}(\mathbf{Q}, T) = \frac{M_0 N_p^{-1}}{\sqrt{M_\kappa M_{\kappa'}}} \sum_{\mathbf{q}\nu} \langle u_{\mathbf{q}\nu}^2 \rangle_T \text{Re} \left[\mathbf{Q} \cdot \mathbf{e}_{\kappa,\nu}(\mathbf{q}) \mathbf{Q} \cdot \mathbf{e}_{\kappa',\nu}^*(\mathbf{q}) e^{i\mathbf{q} \cdot \mathbf{R}_p} \right], \quad (4)$$

where M_κ and M_0 are the atomic and reference masses, and the phonons are described by the eigenmodes $\mathbf{e}_{\kappa,\nu}(\mathbf{q})$ and frequencies $\omega_{\mathbf{q}\nu}$. A key quantity entering the equation of the structure factor is the mean-squared displacement of the atoms due to mode $\mathbf{q}\nu$, defined as $\langle u_{\mathbf{q}\nu}^2 \rangle_T = \hbar / (2M_0 \omega_{\mathbf{q}\nu}) [2n_{\mathbf{q}\nu}(T) + 1]$. The time-dependence of the all-phonon structure factor is encoded in $\langle u_{\mathbf{q}\nu}^2 \rangle_T$, which is directly related to phonon populations $n_{\mathbf{q}\nu}(T)$. To account for the influence of the non-equilibrium lattice dynamics on the FEDS intensity, we evaluated Eq. (3) at each time snapshot by populating phonons according to the vibrational temperatures obtained from the solution of the time-dependent Boltzmann equation (Figure 4).

The calculated (non-equilibrium) all-phonon structure factor is shown in Figure 3 (d) for $t = 2$ ps. The intensity is relative to equilibrium at 100 K. The calculation agrees well with the experimental FEDS intensity reported in Figure 3 (a) and it reproduces the main fingerprints of non-equilibrium lattice dynamics. In particular, the faint vertical high-intensity features which connect the Bragg peaks across different BZ – and constitute a striking manifestation of the non-equilibrium state of the lattice – are well captured by the simulations. The time dependence of the vibrational temperature in the BZ, illustrated in Figure 4, enable us to attribute these features to the higher population of phonons along the Γ -A direction which, in turn, arises from the primary role played by these phonons in the relaxation of the excited electronic distribution. The calculated FEDS intensities at 10 ps and 50 ps, shown in Figure 3 (b) and (c), respectively, further capture the emergence of a

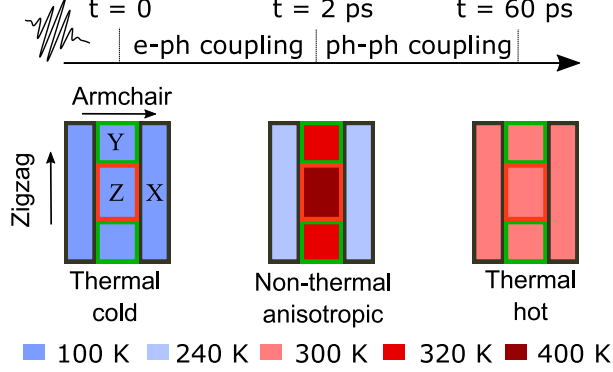


Figure 5: Sketch of the non-equilibrium dynamics and thermalization of the BP lattice following photo-excitation.

diamond-shaped diffraction pattern that characterises the return to thermal equilibrium.

These findings enable us to establish the picture sketched in Figure 5 for the non-equilibrium dynamics and thermalization of vibrational degrees of freedom in BP: After the creation of an excited electronic distribution by a laser pulse, electrons (holes) in the conduction (valence) band undergo electron-electron scattering and occupy the band edges according to Fermi-Dirac statistics. This results into a highly anisotropic distribution of photo-excited carriers in the BZ, predominantly populating the Z, Y, A, and A' pockets. Within 2 ps after photo-excitation, electrons and holes lose their excess energy upon emitting phonons. Momentum selectivity in the phonon emission leads to the primary excitation of phonons with momenta along the zigzag direction of the crystal, driving the lattice into a non-equilibrium regime characterized by a highly-anisotropic phonon population in the BZ (Figure 4(b-d)). Distinctive fingerprints of this regime are visible in the FEDS intensity at $t = 2$ ps (Figure 3(b)). The ensuing *hot*-phonon population subsequently thermalizes with other lattice vibrations via phonon-phonon scattering, thereby driving the lattice towards thermal equilibrium (i.e., $T_{\mathbf{q}\nu} = \text{const.}$) within 50 ps, and leading to the thermalized FEDS intensity reported in Figure 3(c).

Conclusions

We have provided a comprehensive picture of the microscopic energy flows in the crystal lattice of BP following photo-excitation of the electrons. The time- and momentum-resolved diffuse scattering experiments have revealed that highly-anisotropic transient phonon populations are established upon photo-excitation. By accounting explicitly for electron-phonon and phonon-phonon scattering within an ab-initio theoretical description of the coupled electron-phonon dynamics, we have demonstrated that this behaviour can be attributed to the preferential emission of high energy optical phonons along the zigzag direction of the BP lattice throughout the relaxation of the photo-excited electronic distribution. This picture is corroborated by the good agreement between the calculated all-phonon structure factors and the measured FEDS intensity throughout the different stages of the non-equilibrium dynamics of the lattice. Our approach can be extended to 2D materials, and could be exploited more broadly in many areas of material sciences and condensed matter physics, ranging from transport to superconductivity phenomena. For instance, it could be employed to reveal energy transfer pathways accross interfaces in van der Waals heterostructures, or to identify specific phonons involved in complex electron-phonon dynamical processes such as polaron formation or phase transitions.

Methods

Sample preparation and thickness determination

The thin black phosphorus (BP) flake was obtained by standard mechanical exfoliation performed in air. The samples were then quickly imaged in the optical microscope and subsequently transferred to a load-lock chamber connected to our main experimental chamber in ultra-high vacuum. We estimate the total exposure to air to be less than one hour. We found that this method yielded diffraction patterns consistent with previous experimental

works.³¹ Given the multilayer nature of the samples (40 nm corresponds to roughly 80 layers), the observed scattering signals predominantly arise from the bulk as opposed to the oxidized surface layers of the flake. We note, however, the presence of forbidden reflections ($h + l = 2n + 1$) in the diffraction patterns. Such forbidden reflections were also observed in previous works, but their origin could not be attributed with certainty.³¹ We postulate that they may be caused by stacking faults or structural deviations at the surface. These additional reflections do not alter the overall agreement between experiment and theory.

The flake thickness was estimated by transmission measurements in an optical microscope in combination with transfer matrix calculations and the optical constants of BP.¹⁷

Computational details

First-principles calculations employed the primitive cell of bulk BP (point group D_{2h} and space group Cmce) that contains 4 atoms.³⁰ All calculations were performed using the PBE generalized gradient approximation⁴¹ to density functional theory. We employed planewaves basis sets and Troullier-Martins norm-conserving pseudopotentials⁴² as implemented in the `Quantum ESPRESSO` suite.⁴³ The planewaves kinetic energy cutoff was set to 90 Ry and the sampling of the Brillouin zone was performed using a uniform $12 \times 10 \times 10$ \mathbf{k} -point grid. We determine the interatomic force constants by means of density-functional perturbation theory calculations⁴⁴ using a $5 \times 5 \times 5$ Brillouin-zone \mathbf{q} -grid. The full set of phonon eigenmodes and eigenfrequencies was obtained by using standard Fourier interpolation of dynamical matrices on a $50 \times 50 \times 50$ \mathbf{q} -point grid. Such a dense grid guarantees a fine resolution of the calculated structure factor maps. The phonon band structure over a chosen high-symmetry path is shown in Figure S2.

Acknowledgement

This work was funded by the Max Planck Society, the European Research Council (ERC) under the European Union's Horizon 2020 research and innovation program (Grant Agreement Number ERC-2015-CoG-682843), and partially by the Deutsche Forschungsgemeinschaft (DFG) - Projektnummer 182087777 - SFB 951. F.C. acknowledges funding by the DFG – Projektnummer 443988403. H.S. acknowledges support by the Swiss National Science Foundation under Grant No. P2SKP2_184100. M.Z. acknowledges financial support from the Research Unit of Nanostructured Materials Systems (RUNMS) and program ΜΕΤΑΔΙΔΑΚΤΩΡ. Y.Q. acknowledges support by the Sino-German (CSC-DAAD) Postdoc Scholarship Program (Grant No. 57343410). Y.W.W acknowledges funding from the DFG within the Emmy Noether program under Grant No. RE 3977/1. We thank Maciej Dendzik for helpful discussions, and Laurent René de Cotret for his open-source software. F.C. and C.D. acknowledge Dino Novko for useful discussions.

Supporting Information Available

Estimation of excited carrier density; Diffuse scattering maps: raw data and influence of pump photon energy

References

- (1) Qiao, J.; Kong, X.; Hu, Z.-X.; Yang, F.; Ji, W. High-mobility transport anisotropy and linear dichroism in few-layer black phosphorus. *Nature Communications* **2014**, *5*, 4475–.
- (2) Castellanos-Gomez, A. Black Phosphorus: Narrow Gap, Wide Applications. *J. Phys. Chem. Lett.* **2015**, *6*, 4280–4291.

- (3) Li, L.; Kim, J.; Jin, C.; Ye, G. J.; Qiu, D. Y.; da Jornada, F. H.; Shi, Z.; Chen, L.; Zhang, Z.; Yang, F., et al. Direct observation of the layer-dependent electronic structure in phosphorene. *Nature Nanotechnology* **2016**, *12*, 21–.
- (4) Li, L.; Yu, Y.; Ye, G. J.; Ge, Q.; Ou, X.; Wu, H.; Feng, D.; Chen, X. H.; Zhang, Y. Black phosphorus field-effect transistors. *Nature Nanotechnology* **2014**, *9*, 372–.
- (5) Xia, F.; Wang, H.; Jia, Y. Rediscovering black phosphorus as an anisotropic layered material for optoelectronics and electronics. *Nature Communications* **2014**, *5*.
- (6) Long, G.; Maryenko, D.; Shen, J.; Xu, S.; Hou, J.; Wu, Z.; Wong, W. K.; Han, T.; Lin, J.; Cai, Y., et al. Achieving Ultrahigh Carrier Mobility in Two-Dimensional Hole Gas of Black Phosphorus. *Nano Letters* **2016**, *16*, 7768–7773.
- (7) Ling, X.; Wang, H.; Huang, S.; Xia, F.; Dresselhaus, M. S. The renaissance of black phosphorus. *Proceedings of the National Academy of Sciences* **2015**, *112*, 4523–4530.
- (8) Buscema, M.; Groenendijk, D. J.; Blanter, S. I.; Steele, G. A.; van der Zant, H. S. J.; Castellanos-Gomez, A. Fast and Broadband Photoresponse of Few-Layer Black Phosphorus Field-Effect Transistors. *Nano Letters* **2014**, *14*, 3347–3352.
- (9) Sotor, J.; Sobon, G.; Macherzynski, W.; Paletko, P.; Abramski, K. M. Black phosphorus saturable absorber for ultrashort pulse generation. *Applied Physics Letters* **2015**, *107*, 051108.
- (10) Lee, S.; Yang, F.; Suh, J.; Yang, S.; Lee, Y.; Li, G.; Sung Choe, H.; Suslu, A.; Chen, Y.; Ko, C., et al. Anisotropic in-plane thermal conductivity of black phosphorus nanoribbons at temperatures higher than 100 K. *Nature Communications* **2015**, *6*, 8573–.
- (11) Luo, Z.; Maassen, J.; Deng, Y.; Du, Y.; Garrelts, R. P.; Lundstrom, M. S.; Ye, P. D.; Xu, X. Anisotropic in-plane thermal conductivity observed in few-layer black phosphorus. *Nature Communications* **2015**, *6*, 8572.

- (12) Jang, H.; Wood, J. D.; Ryder, C. R.; Hersam, M. C.; Cahill, D. G. Anisotropic Thermal Conductivity of Exfoliated Black Phosphorus. *Advanced Materials* **2015**, *27*, 8017–8022.
- (13) Liu, H.; Neal, A. T.; Zhu, Z.; Luo, Z.; Xu, X.; Tománek, D.; Ye, P. D. Phosphorene: An Unexplored 2D Semiconductor with a High Hole Mobility. *ACS Nano* **2014**, *8*, 4033–4041.
- (14) He, J.; He, D.; Wang, Y.; Cui, Q.; Bellus, M. Z.; Chiu, H.-Y.; Zhao, H. Exceptional and Anisotropic Transport Properties of Photocarriers in Black Phosphorus. *ACS Nano* **2015**, *9*, 6436–6442.
- (15) Tran, V.; Soklaski, R.; Liang, Y.; Yang, L. Layer-controlled band gap and anisotropic excitons in few-layer black phosphorus. *Phys. Rev. B* **2014**, *89*, 235319.
- (16) Low, T.; Rodin, A. S.; Carvalho, A.; Jiang, Y.; Wang, H.; Xia, F.; Castro Neto, A. H. Tunable optical properties of multilayer black phosphorus thin films. *Phys. Rev. B* **2014**, *90*, 075434.
- (17) Jiang, H.; Shi, H.; Sun, X.; Gao, B. Optical Anisotropy of Few-Layer Black Phosphorus Visualized by Scanning Polarization Modulation Microscopy. *ACS Photonics* **2018**, *5*, 2509–2515.
- (18) Ge, S.; Li, C.; Zhang, Z.; Zhang, C.; Zhang, Y.; Qiu, J.; Wang, Q.; Liu, J.; Jia, S.; Feng, J.; Sun, D. Dynamical Evolution of Anisotropic Response in Black Phosphorus under Ultrafast Photoexcitation. *Nano Letters* **2015**, *15*, 4650–4656.
- (19) Suess, R. J.; Jadidi, M. M.; Murphy, T. E.; Mittendorff, M. Carrier dynamics and transient photobleaching in thin layers of black phosphorus. *Applied Physics Letters* **2015**, *107*, 081103.

- (20) Wang, K.; Szydłowska, B. M.; Wang, G.; Zhang, X.; Wang, J. J.; Magan, J. J.; Zhang, L.; Coleman, J. N.; Wang, J.; Blau, W. J. Ultrafast Nonlinear Excitation Dynamics of Black Phosphorus Nanosheets from Visible to Mid-Infrared. *ACS Nano* **2016**, *10*, 6923–6932.
- (21) Iyer, V.; Ye, P.; Xu, X. Mid-infrared ultrafast carrier dynamics in thin film black phosphorus. *2D Materials* **2017**, *4*, 021032.
- (22) Liao, B.; Zhao, H.; Najafi, E.; Yan, X.; Tian, H.; Tice, J.; Minnich, A. J.; Wang, H.; Zewail, A. H. Spatial-Temporal Imaging of Anisotropic Photocarrier Dynamics in Black Phosphorus. *Nano Letters* **2017**, *17*, 3675–3680.
- (23) Meng, S.; Shi, H.; Jiang, H.; Sun, X.; Gao, B. Anisotropic Charge Carrier and Coherent Acoustic Phonon Dynamics of Black Phosphorus Studied by Transient Absorption Microscopy. *The Journal of Physical Chemistry C* **2019**, *123*, 20051–20058.
- (24) Roth, S.; Crepaldi, A.; Puppini, M.; Gatti, G.; Bugini, D.; Grimaldi, I.; Barrilot, T. R.; Arrell, C. A.; Frassetto, F.; Poletto, L., et al. Photocarrier-induced band-gap renormalization and ultrafast charge dynamics in black phosphorus. *2D Materials* **2019**, *6*, 031001.
- (25) Chen, Z.; Dong, J.; Papalazarou, E.; Marsi, M.; Giorgetti, C.; Zhang, Z.; Tian, B.; Rueff, J.-P.; Taleb-Ibrahimi, A.; Perfetti, L. Band Gap Renormalization, Carrier Multiplication, and Stark Broadening in Photoexcited Black Phosphorus. *Nano Letters* **2019**, *19*, 488–493.
- (26) Stern, M. J.; de Cotret, L. P. R.; Otto, M. R.; Chatelain, R. P.; Boisvert, J.-P.; Sutton, M.; Siwick, B. J. Mapping momentum-dependent electron-phonon coupling and nonequilibrium phonon dynamics with ultrafast electron diffuse scattering. *Physical Review B* **2018**, *97*.

- (27) de Cotret, L. P. R.; Pöhls, J.-H.; Stern, M. J.; Otto, M. R.; Sutton, M.; Siwick, B. J. Time- and momentum-resolved phonon population dynamics with ultrafast electron diffuse scattering. *Physical Review B* **2019**, *100*.
- (28) Waldecker, L.; Bertoni, R.; Huebener, H.; Brumme, T.; Vasileiadis, T.; Zahn, D.; Rubio, A.; Ernstorfer, R. Momentum-Resolved View of Electron-Phonon Coupling in Multilayer WSe₂. *Phys. Rev. Lett.* **2017**, *119*.
- (29) Keyes, R. W. The Electrical Properties of Black Phosphorus. *Physical Review* **1953**, *92*, 580–584.
- (30) Ribeiro, H. B.; Pimenta, M. A.; de Matos, C. J. Raman spectroscopy in black phosphorus. *Journal of Raman Spectroscopy* **2018**, *49*, 76–90.
- (31) Castellanos-Gomez, A.; Vicarelli, L.; Prada, E.; Island, J. O.; Narasimha-Acharya, K. L.; Blanter, S. I.; Groenendijk, D. J.; Buscema, M.; Steele, G. A.; Alvarez, J. V., et al. Isolation and characterization of few-layer black phosphorus. *2D Materials* **2014**, *1*, 025001.
- (32) Waldecker, L.; Bertoni, R.; Ernstorfer, R. Compact femtosecond electron diffractometer with 100 keV electron bunches approaching the single-electron pulse duration limit. *Journal of Applied Physics* **2015**, *117*, 044903.
- (33) Zahn, D.; Hildebrandt, P.-N.; Vasileiadis, T.; Windsor, Y. W.; Qi, Y.; Seiler, H.; Ernstorfer, R. Anisotropic Nonequilibrium Lattice Dynamics of Black Phosphorus. *Nano Letters* **2020**, *20*, 3728–3733.
- (34) Trigo, M.; Chen, J.; Vishwanath, V. H.; Sheu, Y. M.; Graber, T.; Henning, R.; Reis, D. A. Imaging nonequilibrium atomic vibrations with x-ray diffuse scattering. *Phys. Rev. B* **2010**, *82*, 235205.

- (35) Trigo, M.; Fuchs, M.; Chen, J.; Jiang, M. P.; Cammarata, M.; Fahy, S.; Fritz, D. M.; Gaffney, K.; Ghimire, S.; Higginbotham, A., et al. Fourier-transform inelastic X-ray scattering from time- and momentum-dependent phonon–phonon correlations. *Nature Physics* **2013**, *9*, 790–794.
- (36) Wall, S.; Yang, S.; Vidas, L.; Chollet, M.; Glowina, J. M.; Kozina, M.; Katayama, T.; Henighan, T.; Jiang, M.; Miller, T. A., et al. Ultrafast disordering of vanadium dimers in photoexcited VO₂. *Science* **2018**, *362*, 572–576.
- (37) Caruso, F. Nonequilibrium Lattice Dynamics in Monolayer MoS₂. *The Journal of Physical Chemistry Letters* **2021**, *12*, 1734–1740, PMID: 33569950.
- (38) de Cotret, L. P. R.; Otto, M. R.; Stern, M. J.; Siwick, B. J. An open-source software ecosystem for the interactive exploration of ultrafast electron scattering data. *Advanced Structural and Chemical Imaging* **2018**, *4*.
- (39) Zacharias, M.; Seiler, H.; Caruso, F.; Zahn, D.; Giustino, F.; Kelires, P. C.; Ernstorfer, R. First-principles calculation of the all-phonon inelastic scattering in solids. 2021.
- (40) Zacharias, M.; Seiler, H.; Caruso, F.; Zahn, D.; Giustino, F.; Kelires, P. C.; Ernstorfer, R. Multi-phonon diffuse scattering in solids from first-principles: Application to 2D MoS₂, bulk MoS₂, and black Phosphorous. 2021.
- (41) Perdew, J. P.; Burke, K.; Ernzerhof, M. Generalized Gradient Approximation Made Simple. *Phys. Rev. Lett.* **1996**, *77*, 3865–3868.
- (42) Troullier, N.; Martins, J. L. Efficient pseudopotentials for plane-wave calculations. *Phys. Rev. B* **1991**, *43*, 1993–2006.
- (43) Giannozzi, P. et al. QUANTUM ESPRESSO: a modular and open-source software project for quantum simulations of materials. *J. Phys.: Condens. Matter* **2009**, *21*, 395502.

- (44) Baroni, S.; de Gironcoli, S.; Dal Corso, A.; Giannozzi, P. Phonons and related crystal properties from density-functional perturbation theory. *Rev. Mod. Phys.* **2001**, *73*, 515–562.

Supporting Information:

Accessing the anisotropic non-equilibrium phonon populations in black phosphorus

Hélène Seiler,^{*,†} Daniela Zahn,[†] Marios Zacharias,^{†,‡} Patrick Hildebrandt,[†]
Thomas Vasileiadis,[†] Yoav William Windsor,[†] Yingpeng Qi,[†] Christian Carugno,[†]
Claudia Draxl,[¶] Ralph Ernstorfer,[†] and Fabio Caruso^{*,§}

[†]*Fritz Haber Institute of the Max Planck Society, 14195 Berlin, Germany*

[‡]*Department of Mechanical and Materials Science Engineering, Cyprus University of
Technology, P.O. Box 50329, 3603 Limassol, Cyprus*

[¶]*Institut für Physik and IRIS Adlershof, Humboldt-Universität zu Berlin, Berlin, Germany*

[§]*Institut für Theoretische Physik und Astrophysik, Christian-Albrechts-Universität zu Kiel,
D-24098 Kiel, Germany*

E-mail: seiler@fhi-berlin.mpg.de; caruso@physik.uni-kiel.de

Estimation of excited carrier density

The incident fluence on the BP flake is $I_{\text{inc}} = 98 \text{ J/m}^2$. The pump was polarized along the *armchair* direction, determined by rotating a waveplate in the pump arm and maximizing the Debye-Waller effect at 50 ps (maximum absorption). Given the highly anisotropic optical absorption of BP, specifying the pump polarization is essential to employ the proper value of refractive index, which matters for the estimation of excited carrier density. The complex refractive index of BP along the *armchair* direction at 800 nm is $3.19 + 0.29i$, as estimated from a previous work.¹ We use transfer matrices to calculate the transmitted part, T , as well as the reflected part, R , of the incident fluence. This yields the absorbed fluence $I_{\text{abs}} = (1 - R - T) \cdot I_{\text{inc}}$. The carrier density per square centimeter is then:

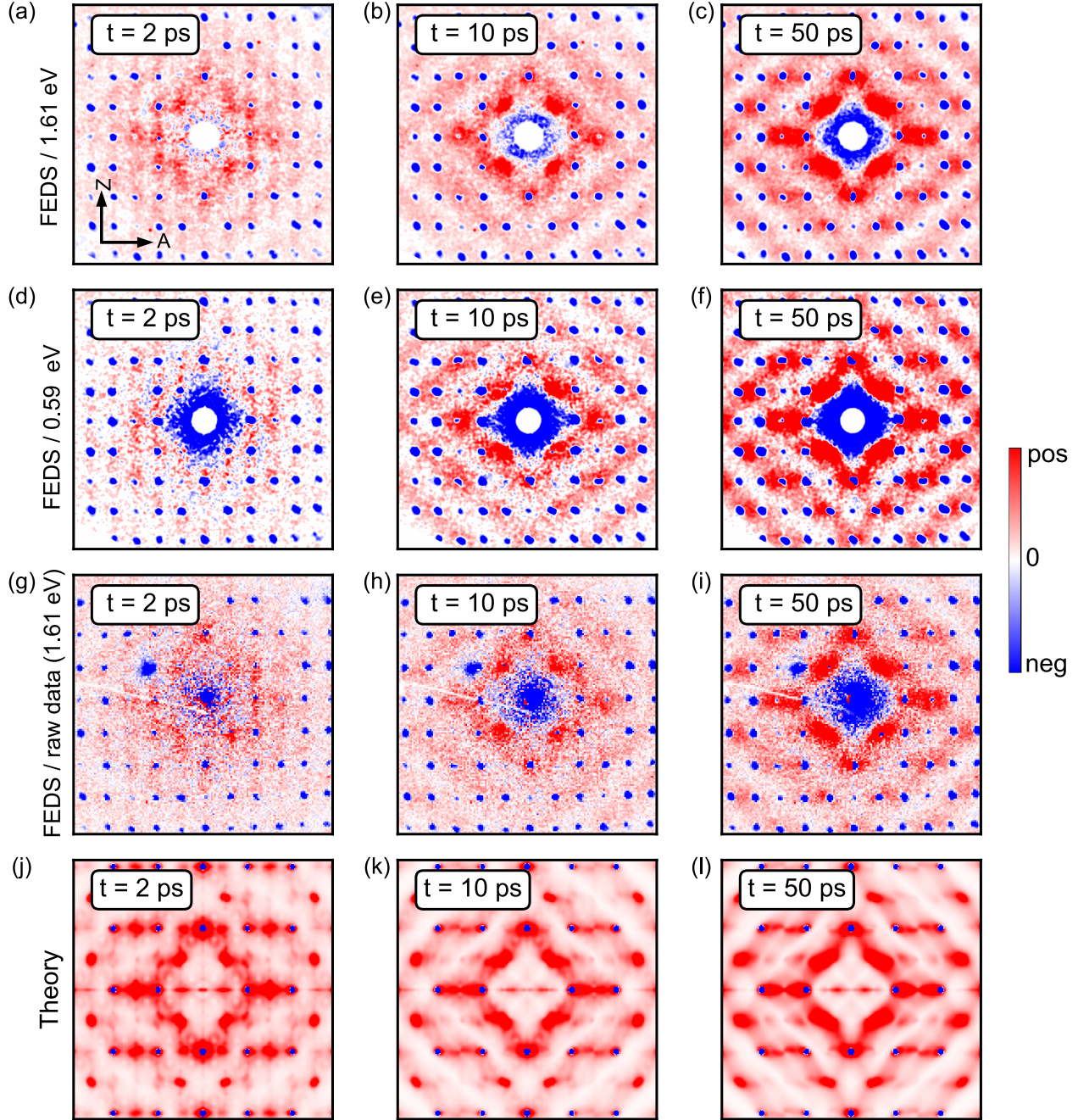
$$n = 10^{-6} \cdot \frac{1}{E_{\text{ph}}} \cdot \frac{I_{\text{abs}}}{d} \cdot c \cdot \frac{1}{2} = (7.3 \pm 0.9) \cdot 10^{13} \text{ electrons/cm}^2,$$

where E_{ph} is the energy of one pump photon, d is the flake thickness, which we estimate to $39 \pm 5 \text{ nm}$, $c = 10.46 \cdot 10^{-10} \text{ m}$ is the unit cell length in the out-of-plane direction and the factor $1/2$ accounts for the two layers per unit cell.

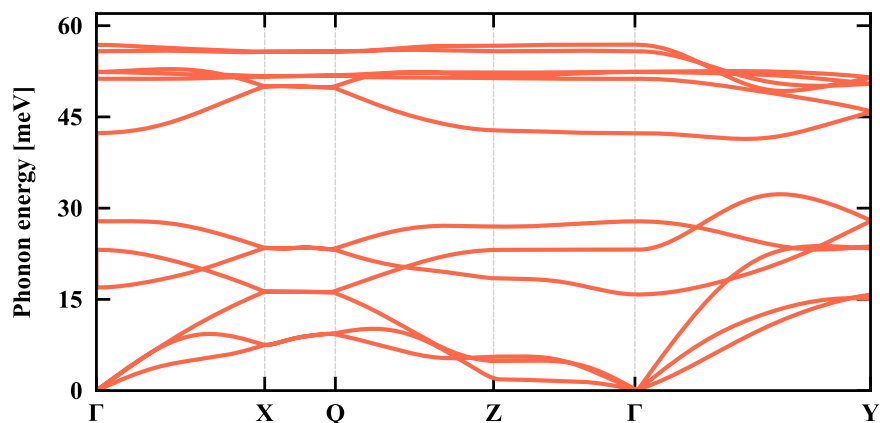
Diffuse scattering maps: raw data and influence of pump photon energy

In supplementary Figure 1 we show a series of diffuse scattering maps at chosen delays and for different pump photon energies and/or data processing steps. Panels (a-c) and (j-l) correspond to the experimental and theoretical results shown in Figure 3 of the main text, respectively. They are reproduced here for convenience. Panels (d-f) display the diffuse scattering signals obtained when pumping the sample with 0.59 eV photons. The same initial excited electron density is assumed for both the 0.59 eV and 1.61 eV experiments, based on the Bragg peaks' reduction at 300 ps. While the diffuse scattering signatures at 2 ps seem slightly more intense for the 1.61 eV pump, we observe the same qualitative thermalization process in both cases. Since the picosecond dynamics does not seem to depend significantly on the initial carrier distribution after excitation, the assumption of a thermalized electron system for our purposes seems justified. In the main text and in panels (a-f), we show two-fold symmetrized data. This processed data is obtained using the open-source Python environment developed by De Cotret et al.² Prior to symmetrization, it was verified that the time-dependence of the elastic scattering for Friedel pairs showed the same dynamics within error margin. The raw data for the 1.61 eV pump are shown in panels (g-i). Comparing panels (a-c) and (g-i), we observe peak splitting effects at large scattering vectors for the symmetrized data. This artifact arises from field distortions of our magnetic lens, which contains aberrations at higher scattering vectors.

Supplementary Figures



Supplementary Figure 1: Diffuse scattering maps at 2 ps, 10 ps, and 50 ps for different pump photon energies and data processing steps. (a-c) Two-fold symmetrized, 1.61 eV pump. (d-f) Two-fold symmetrized, 0.59 eV pump. (g-i) Raw data (binned), 1.67 eV pump. (j-l) Theory results obtained assuming an excited carried density of $1.42 \cdot 10^{21}$ electrons/cm³.



Supplementary Figure 2: Phonon dispersion of BP calculated from density-functional perturbation theory over the Γ -X-Q-Z- Γ -Y path.

References

- (1) Jiang, H.; Shi, H.; Sun, X.; Gao, B. Optical Anisotropy of Few-Layer Black Phosphorus Visualized by Scanning Polarization Modulation Microscopy. *ACS Photonics* **2018**, *5*, 2509–2515.
- (2) de Cotret, L. P. R.; Otto, M. R.; Stern, M. J.; Siwick, B. J. An open-source software ecosystem for the interactive exploration of ultrafast electron scattering data. *Advanced Structural and Chemical Imaging* **2018**, *4*.